ADVANCED ENERGY MATERIALS
www.advenergymat.de

Mechanochemical Synthesis: A Tool to Tune Cation Site Disorder and Ionic Transport Properties of Li_3MCl_6 (M = Y, Er) Superionic Conductors

*Roman Schlem, Sokseiha Muy, Nils Prinz, Ananya Banik, Yang Shao-Horn, Mirijam Zobel, and Wolfgang G. Zeier**

The lithium-conducting, rare-earth halides, Li_3MX_6 (M = Y, Er; X = Cl, Br), have garnered significantly rising interest recently, as they have been reported to have oxidative stability and high ionic conductivities. However, while a multitude of materials exhibit a superionic conductivity close to 1 mS cm^{-1}, the exact design strategies to further improve the ionic transport properties have not been established yet. Here, the influence of the employed synthesis method of mechanochemical milling, compared to subsequent crystallization routines as well as classic solid-state syntheses on the structure and resulting transport behavior of Li_3ErCl_6 and Li_3YCl_6 are explored. Using a combination of X-ray diffraction, pair distribution function analysis, density functional theory, and impedance spectroscopy, insights into the average and local structural features that influence the underlying transport are provided. The existence of a cation defect within the structure in which Er/Y are disordered to a new position strongly benefits the transport properties. A synthetically tuned, increasing degree of this disordering leads to a decreasing activation energy and increasing ionic conductivity. This work sheds light on the possible synthesis strategies and helps to systematically understand and further improve the properties of this class of materials.

1. Introduction

The steadily rising demand for energy storage has led to an increased interest in the field of all solid-state batteries and the field of fast ion-conducting solid electrolytes.[1,2] While the liquid electrolytes that are commonly used in conventional Li-ion batteries contain organic easily flammable solvents, recent progress on solid-electrolyte-based batteries offers the opportunity to explore a safer and similar performing alternative.[3] Prominent representatives are the lithium-conducting garnets such as $Li_7La_3Zr_2O_{12}$,[4–7] thiophosphate-based $Li_{10}GeP_2S_{12}$,[8–12] and halide argyrodites Li_6PS_5X (X = Cl, Br, and I),[13–16] as well as amorphous phases within the Li_2S-P_2S_5 system.[17–22] While these solid electrolytes are being used in solid-state batteries, the interface behavior in contact to different electrode materials and the need for large-scale processability remain a challenge.[23–27] Nevertheless, despite their higher sensitivity to decomposition in atmosphere and at higher oxidative potentials,[28] thiophosphates have shown promising solid-state battery performance because of their mechanically soft nature and improved processability.[12,29,30]

Challenged by the oxidative instability of the thiophosphate-based electrolyte, recently, the rare-earth halides Li_3YX_6 (X = Cl, Br) have attracted interest as they exhibit high ionic conductivity on the order of 1 mS cm^{-1} and have been reported to exhibit an enhanced oxidative stability to higher potentials.[31,32] In addition, by combining multiple descriptors[33] for fast ionic motion along with the need for high stability, Li_3ErCl_6,[33] Li_3LaI_6,[34] and Li_3InCl_6[35] were found to exhibit a high ionic conductivity. However, none of these materials are novel in itself as the work on the A_3InCl_6 (A = Na, K, Ag, Tl) systems dates back as far as 1967.[36] The rare earth analogue containing yttrium (Y) gained interest in 1992,[37] when Steiner et al. identified A_3MCl_6 (A = Li, Na, Ag, M = In, Y) to be good ionic conductors with an ionic conductivity of around 0.2 S cm^{-1} at 300 °C for Li_3InCl_6.

Using single-crystal diffraction data, Steiner et al.[37] proposed an orthorhombic unit cell for Li_3YCl_6 while recent studies suggest a trigonal unit cell for Li_3YCl_6 and the

R. Schlem, Dr. A. Banik, Dr. W. G. Zeier
Institute of Physical Chemistry
Justus-Liebig-University Giessen
Heinrich-Buff-Ring 17, D-35392 Giessen, Germany
E-mail: wolfgang.g.zeier@pc.jlug.de
R. Schlem, Dr. A. Banik, Dr. W. G. Zeier
Center for Materials Research (LaMa)
Justus-Liebig-University Giessen
Heinrich-Buff-Ring 16, D-35392 Giessen, Germany
Dr. S. Muy, Prof. Y. Shao-Horn
Department of Materials Science and Engineering
Massachusetts Institute of Technology
77 Massachusetts Ave., Cambridge, MA 02139, USA
N. Prinz, Prof. M. Zobel
Department of Chemistry
University of Bayreuth
Universitätsstrasse 30, D-95440 Bayreuth, Germany
The ORCID identification number(s) for the author(s) of this article can be found under https://doi.org/10.1002/aenm.201903719.

DOI: 10.1002/aenm.201903719

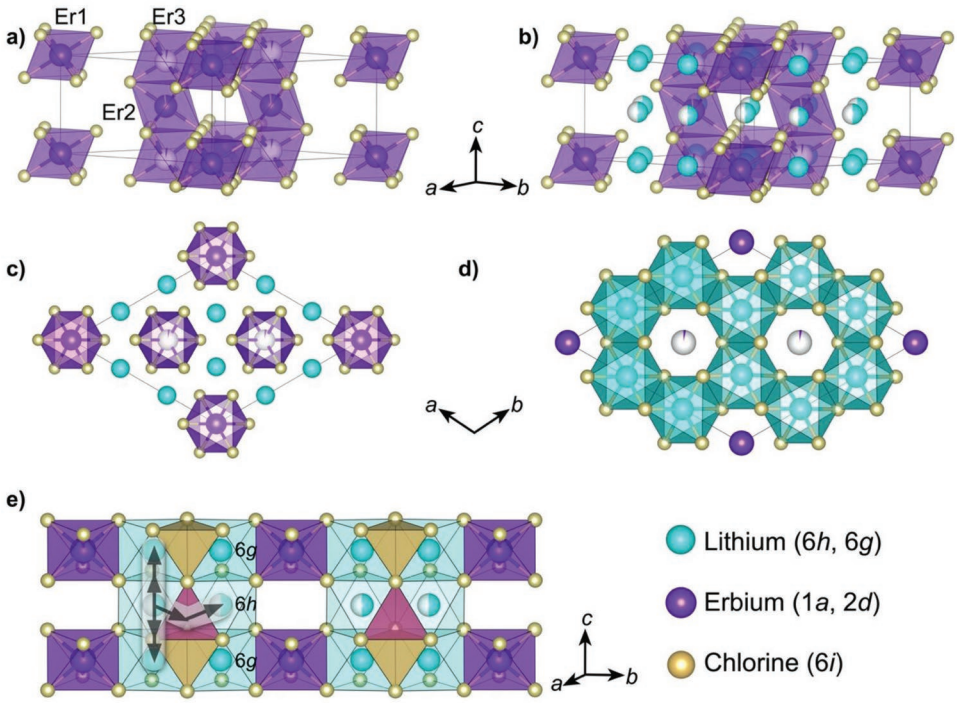

Figure 1. a) Li_3ErCl_6 unit cell with the building units of $ErCl_6^{3-}$ octahedra that form a trigonal unit cell and face-sharing $ErCl_6^{3-}$ octahedra chains perpendicular to the (002) plane, with three possible erbium sites (Er1, Wyckoff 1a and Er2, Er3, Wyckoff 2d). b) Lithium occupies the vacant octahedral sites (Wyckoff 6g (100% occupied), 6h (50% occupied)). c,d) Six edge-sharing $LiCl_6^{5-}$ octahedra surround each $ErCl_6^{3-}$ octahedron in a honeycomb arrangement in the *a*–*b* plane. e) Possible lithium pathways through the face-sharing $LiCl_6^{5-}$ octahedra along the *c*-direction and through a tetrahedral void along the *a*–*b* plane. Within the plane, a wide range lithium ionic transport is likely only mediated by the partially occupied lithium 6h positions.

isostructural Li_3ErCl_6.[31–33] The structures of Li_3MCl_6 (M = Y, Er; space group $P\bar{3}m1$) can be described as MCl_6^{3-} octahedra forming a trigonal lattice (**Figure 1**), where the Wyckoff position 1*a* are occupied by *M*1. In addition, two *M*2 atoms occupy the Wyckoff 2*d* position located in the (002) plane (Figure 1b) and also form MCl_6^{3-} octahedra. In the fully ordered structure the occupancy of *M*2 would be equal to 100%. However, suggested by Asano et al.[31] and previously shown in single-crystal X-ray diffraction,[38] there seems to exist a site disorder, in which some previous *M*2 cations are located on another *M*3 position. This new *M*3 site can be regarded as the *M*2-equivalent position in the (001) plane, i.e., translated by half a unit cell in the *z*-direction (see Figure 1). The existence of this *M*2–*M*3 disorder can be viewed as chains of face-sharing MCl_6^{3-} octahedra perpendicular to the (002) plane (Figure 1c), however, a neighboring occupancy of erbium or yttrium is unlikely due to strong repulsion. Recent experimental work on Li_3YCl_6[31] and Li_3ErCl_6[33] suggests an influence of the synthesis procedure on the site disorder and with a higher disorder a beneficial influence on the ionic transport.[31,33] In contrast, theoretical work suggests that disorder, in this case antisite disorder, is detrimental to the ionic conductivity.[32] However, whereas the experimental work suggests *M*2–*M*3 site disorder, the influence of antisite *M*-Li disorder on the ionic conductivity was explored theoretically and represents a defect model with a blockage of the lithium-diffusion channels.

Within the structure, lithium ions occupy the octahedral voids (Wyckoff 6g and 6h) that are formed by the halide ions. Each MCl_6^{3-} octahedron is surrounded by six lithium ions that form a honeycomb lattice of edge-sharing $LiCl_6^{5-}$ octahedra in the *a*–*b* plane (Figure 1c,d). In addition, based on X-ray diffraction data, it seems that the Li positions on 6g within the (001) plane are fully occupied with a partial occupancy of Li2 on 6h within the (002) plane, suggesting a prevalent diffusion pathway within the (002) plane and along the face-sharing octahedra in the *z*-direction.

Inspired by the fast ion transport,[31,35] the clear but not yet understood influence of the synthesis methods on the ionic transport,[33] and the open question of Y/Er site disorder,[31,33] here we investigate the influence of the synthesis on the local structure and with it the resulting ionic transport properties. Using a combination of X-ray diffraction, X-ray pair distribution function (PDF) analysis, impedance spectroscopy, and density functional theory (DFT), we show the direct influence of the synthesis methods on the local structure and transport properties. While mechanochemical synthesis leads to a high *M*2–*M*3 site disorder up to an almost complete site inversion between the *M*2 and *M*3 site, the classic ampoule syntheses only lead to a low degree of this site disorder. By employing different crystallization times, the *M*2–*M*3 site disorder is further engineered to affect the lithium-ion transport. This work shows that the synthesis approach affects the local structure, local cationic ordering, and ultimately the ionic transport in these halide-based ionic conductors Li_3MCl_6 (M = Y, Er).

2. Results

2.1. Influence of Synthesis on the Structure and Disorder

In order to study the influence of the preparation technique on the resulting transport properties, multiple samples of Li_3ErCl_6 and Li_3YCl_6 were synthesized by either a classic solid-state reaction in a quartz ampoule or a mechanochemical approach in a planetary ball mill. In addition, the milled samples were subjected to a subsequent crystallization step with two different crystallization times of 1 min and 1 h for Li_3ErCl_6. In the case of Li_3YCl_6, a longer crystallization time of 5 min was needed to crystallize the materials (see Figure S1, Supporting Information). As Li_3ErCl_6 and Li_3YCl_6 are isostructural and the ionic radii of Er (89 pm) and Y (90 pm) are nearly identical,[39] the following discussion will only involve the data collected for Li_3ErCl_6 unless indicated otherwise. All results for Li_3YCl_6 are shown complementary in the Supporting Information.

X-ray diffraction data were measured to gain insight into the average structure (see **Figure 2**a). As expected, ball milling leads to a strong broadening of the reflections related to an occurring amorphization. Rietveld refinements of all the crystalline compounds are possible and a representative diffraction pattern of Li_3ErCl_6 crystallized in 1 h can be found in Figure 2c. The obtained refinement results (lattice parameters and site occupancies) for Li_3ErCl_6 and Li_3YCl_6 are given in the Supporting Information. The Rietveld refinement results against the X-ray diffraction data show Er2–Er3 disorder that is the lowest with 2.5(1)% for the classic solid-state synthesis and is significantly higher 9.9(2)% in the ball-milled sample with a subsequent crystallization time of 1 min. Whereas a *M*2–*M*3 site disorder can be found here, any refinement models that include antisite disorder between *M* and Li do not lead to a significant fraction of electron density of Er on the Li positions and antisite disorder can be excluded in the here-investigated materials.

The pair distribution functions $G(r)$ of all samples can be found in Figure 2b for Li_3ErCl_6 along with a representative refinement after a 1 h crystallization time in Figure 2d. When comparing the pair distribution functions, a decaying peak intensity in the ball-milled (as prepared) $G(r)$ can be found,

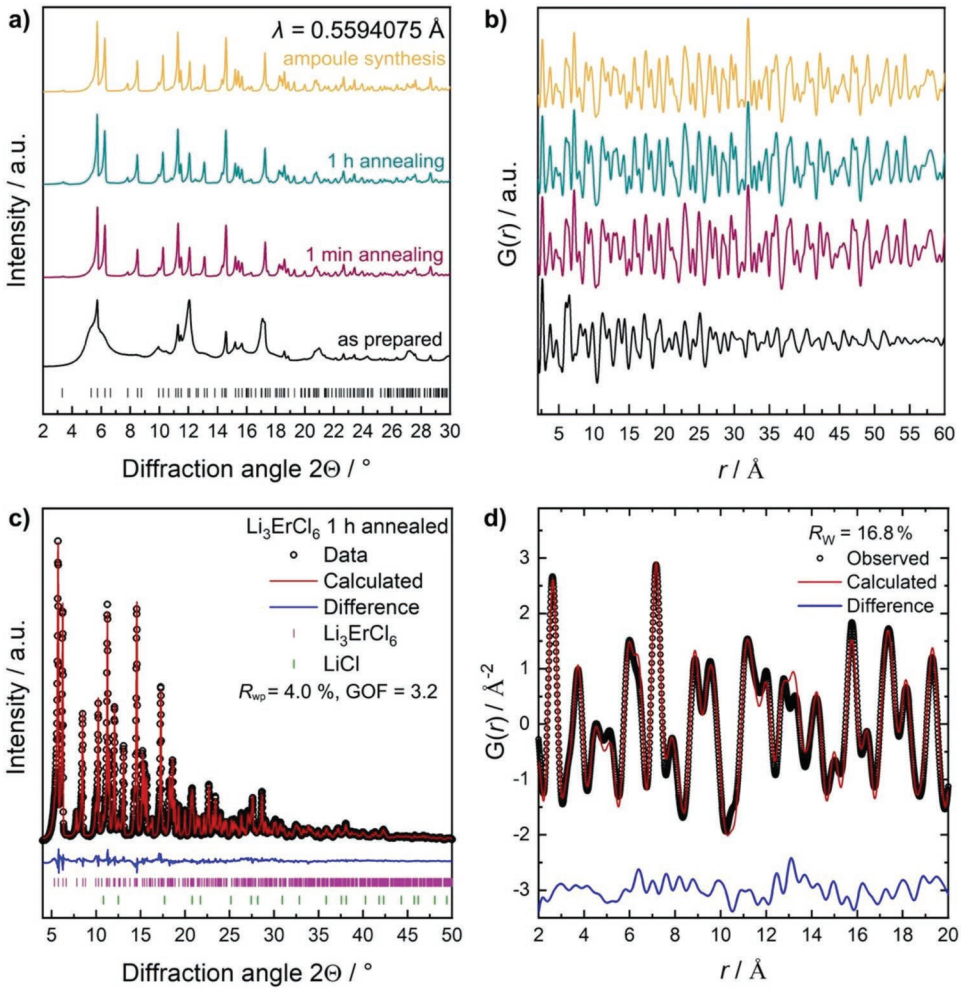

Figure 2. a) Collected X-ray diffraction data and b) calculated pair distribution function $G(r)$ for differently prepared Li_3ErCl_6 samples. c) Additionally, an example Rietveld refinement against the collected X-ray diffraction data and d) fit for the corresponding, calculated $G(r)$ are shown. While the as-prepared sample shows broad reflections indicating a strong amorphization during ball milling, a seemingly complete crystallization of the ball-milled sample can be achieved within 1 min as observable in the diffraction data and respective $G(r)$.

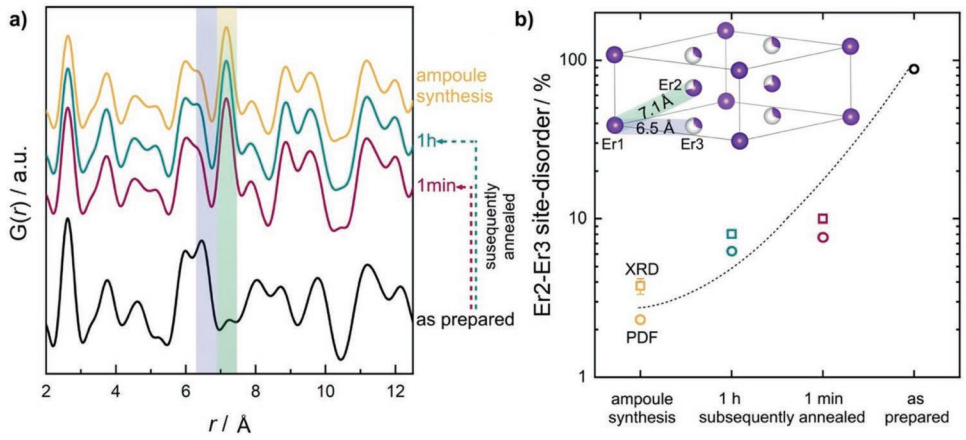

Figure 3. a) Comparison of the pair distribution function $G(r)$ of differently prepared Li_3ErCl_6 samples and b) evolution of the Er2–Er3 site disorder as obtained from $G(r)$ fits (open circles) and Rietveld refinements (open squares). The Er distances are highlighted in the calculated $G(r)$ (a) and the inset of (b).

indicating a lower coherence range in comparison to the annealed samples, further corroborating a lower crystallinity of the materials. However, even within a low *r*-range up to 8 Å, the peak positions in the $G(r)$ suggest that locally Li_3ErCl_6 has already been formed during the milling process, explaining how a short crystallization time of 1 min can even lead to a fully crystalline material. However, a certain phase fraction of the precursor $ErCl_3$ can still be found (see Table S1, Supporting Information). Exceeding the range of 8 Å, the remaining, more crystalline precursor $ErCl_3$ dominates the $G(r)$ due to the low coherence length of the locally formed Li_3ErCl_6. This rapid crystallization within 1 min after mechanochemical milling, while surprising, was recently found to also occur in Li_6PS_5Br,[40] providing further evidence that mechanochemical milling already acts as a primary synthesis step leading to low coherency products and possible prenucleation clusters.

When considering the $G(r)$ at a low *r*-range some interesting trends can be found. The peak corresponding to the Er1–Er2 distance of around 7.1 Å is not yet present in the ball-milled (as prepared) sample, while the distance at around 6.5 Å corresponding to the Er1–Er3 distance shows higher intensity compared to the annealed samples (**Figure 3**a). Qualitatively, these changes in the intensities may be correlated to a *M*2–*M*3 site disorder from the aforementioned Er2 to the Er3 site during the ball-milling process.

Quantitatively, the refinements of the $G(r)$ show similar trends as the Rietveld refinements above. A site disorder between Er2–Er3 of different percentages can be observed for all samples corroborating that the site disorder is strongly dependent on the crystallization time and synthesis procedure. The varying degree of the ordering is shown in Figure 3b, with all exact values provided in Table S2 (Supporting Information). In addition to the changing disorder, annealing leads to a certain degree of microstructural relaxation as indicated by the reduction of the slope in the Williamson–Hall plots in Figure S2 (Supporting Information).

Overall, the structural analyses via Rietveld refinements and pair distribution function analyses show that with increasing annealing time, the Er2–Er3 site disorder decreases from having an almost full disorder after milling. Hence, by applying elevated temperatures, the degree of disorder changes over time and relaxes into a more, but not yet fully ordered structure.

2.2. The Influence of Synthesis on the Polyhedral Pathways

In addition to the changing site disorder, local distortions of the polyhedra can be found using the pair distribution function analyses. These deformations can be visualized using the triangular transition areas that correspond to the bottleneck for lithium diffusion (shown in **Figure 4**a) assuming jumps from one polyhedron to the next. The lithium positions and occupancies remain unknown due to the lack of neutron diffraction data and these triangular transition areas are based on the Er and Cl positions that will influence the resulting lithium diffusion behavior.

There are four different jumps possible for diffusion among connected polyhedra: 1) jumps along the *z*-direction of face-sharing $LiCl_6^{5-}$ octahedra, denoted as O_h (6h)–O_h (6g) jump. Two possible jumps within the *a*–*b* plane in which the $LiCl_6^{5-}$ octahedra are connected via edges and jumps need to occur via a tetrahedral transition state.[41] 2) Jumps are possible in the (002) plane which will include the jump from 6h to 6h, here denoted as O_h (6h)–T_d–O_h (6h) jump, as well as 3) in the (001) plane which will include the jump from 6g to 6g, here denoted as O_h (6g)–T_d–O_h (6g) jump. 4) A fourth jump from T_d–T_d is possible, but improbable as it corresponds to a jump from one transition state to another. While a full occupancy of the 6g makes O_h (6g)–T_d–O_h (6g) unfavorable and unlikely, faster anisotropic diffusion might occur via O_h (6g)–O_h (6h) and O_h (6h)–T_d–O_h (6h).[32]

Figure 4b shows the four different possible polyhedral transition areas as a function of the obtained Er2–Er3 site disorder and corresponding synthesis methods. While the transition areas between the two tetrahedral sites (T_d–T_d) and the two possible octahedral lithium sites (O_h–O_h, 6h–6g) show no visible change for the annealed samples, a large increase of the areas can be observed for the ball-milled (as-prepared) sample. In addition, the transition areas along the *a*–*b* plane

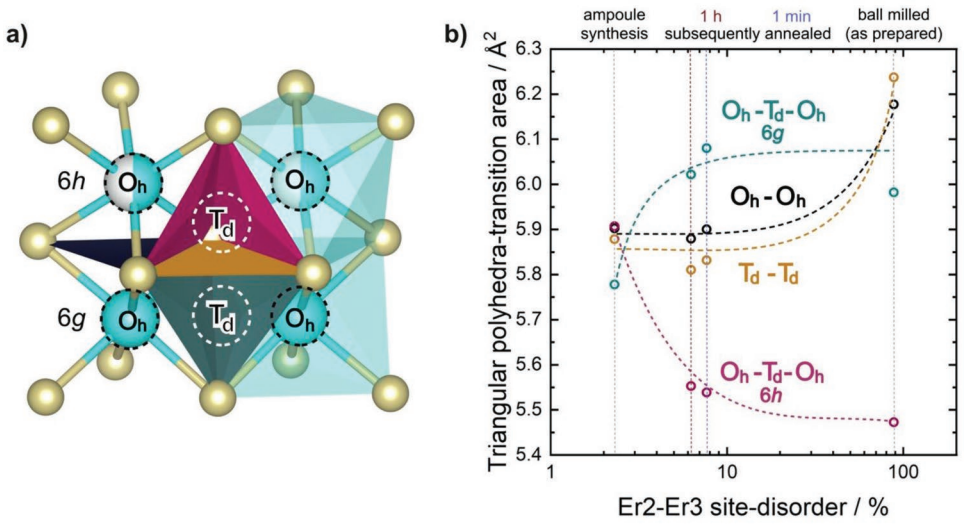

Figure 4. a) Different transition areas for possible lithium diffusion and b) preparation method induced local deformation of structural features. A clear correlation of the obtained Er2–Er3 site disorder can be observed for each of the transition areas. Mechanochemical milling introduces local distortions of the structure that can be visualized using the triangular polyhedral-transition areas, which are ultimately related to the lithium diffusion pathway.

(O_h–T_d–O_h) change significantly with the employed synthesis method. Whereas the transition area of the jump O_h (6g)–T_d–O_h (6g) decreases with increasing annealing time, the area along O_h (6h)–T_d–O_h (6h) increases. The large difference between the polyhedra around Wyckoff 6h and 6g in the ball-milled samples suggests that Er disordering leads to strong local distortions, which in turn will likely affect the lithium occupancies due to Coulombic repulsion. Whereas this relationship becomes clear for Li_3ErCl_6, an assessment of the local polyhedral changes in Li_3YCl_6 is not possible due to a large fluorescence-like behavior (see the Experimental Section).

2.3. Energetics of Various Defect Models

Density functional theory was used to assess the thermodynamic possibility of site disorder. **Figure 5** shows four possible defect models in a 1 × 1 × 2 supercell with different Er2–Er3 disorder and their corresponding energies. The structural models are as follows: structural model 1 corresponds to a Li_3ErCl_6 with Er1 and Er2 fully occupied and resembles the fully ordered structure. Disorder model 2 corresponds to a complete site inversion between Er2 and Er3 leading to a fully occupied Er3 site and a fully vacant Er2 site. Although this

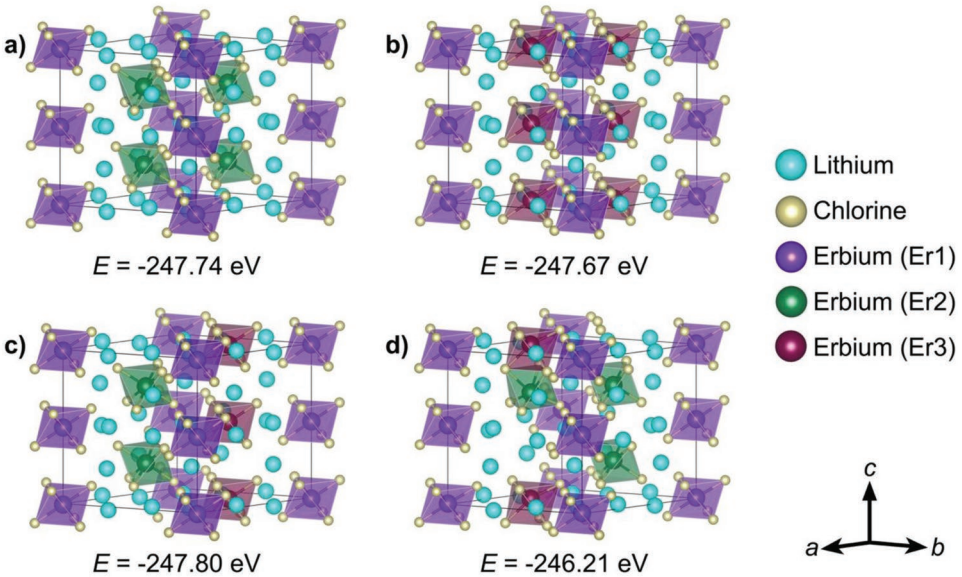

Figure 5. Density functional theory calculated defect models for a 1 × 1 × 2 supercell of Li_3ErCl_6. a,b) Fully occupied Er2 and Er3 sites, fully ordered and fully disordered, respectively, result in a comparable DFT energy and therefore stability for both structures. Although the same holds for (c), the local symmetry reduction for the rotation-inversion center makes this defect model less likely. A mixed defect model including local face-sharing $ErCl_6^{3-}$ octahedra yields the highest energy and lowest stability, possibly related to the resulting strong electrostatic Er2–Er3 repulsion.

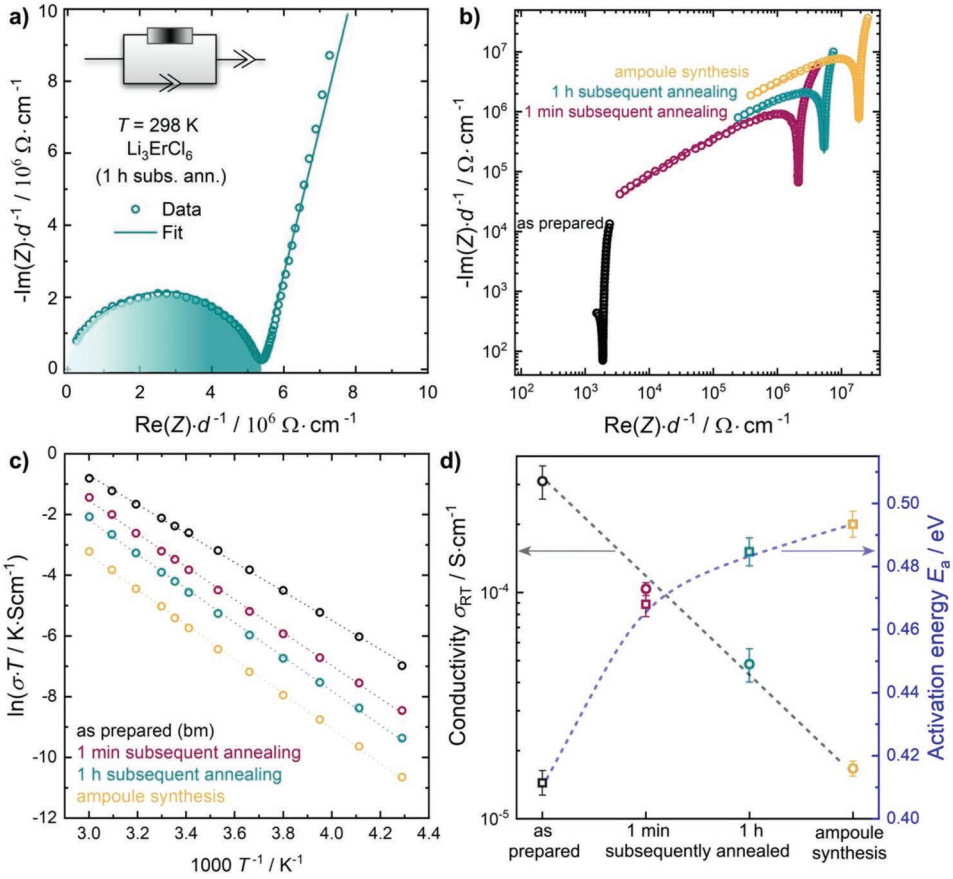

Figure 6. a) Representative Nyquist plot of the 1 h subsequently annealed Li_3ErCl_6 sample, b–d) the comparison of Nyquist plots for the differently prepared samples, normalized to the respective pellet thickness, Arrhenius diagrams, and extracted activation energies as well as the ionic conductivities. With increasing annealing time, the activation energy increases while a decrease of the ionic conductivity can be observed. Open circles correspond to ionic conductivity values and squares to the obtained activation barriers.

model can also be regarded as fully ordered, here, it will be described as fully disordered, respective to the fully ordered model 1. Defect model 3 includes an alternating full Er2 and Er3 site, respectively, while retaining the mirror plane along the (002) plane. This results in a formal, partial occupancy of 50% for both sites. Defect model 4 includes a random occupancy for the Er2 and Er3 sites, resulting in a further reduction of the symmetry and the existence of face-sharing $ErCl_6^{3-}$ octahedra. Similar to Li_3YCl_6 shown by Wang et al.,[32] here density functional theory corroborates that even a structure with full site inversion from Er2 to Er3 (Figure 5a,b) can exhibit similar energies and stabilities as the fully ordered structure. The same holds true for an alternating model 3, with full Er2–Er3 occupancies (Figure 5c). While this structure would result in a strong local symmetry reduction that cannot be captured here experimentally, it clearly shows the possibility of mixed site occupancies. Figure 5d shows model 4 which includes local face-sharing $ErCl_6^{3-}$ octahedra due to the random Er2–Er3 configuration. This model shows the highest energy and therefore lowest stability, likely related to the stronger repulsion of Er2–Er3 as a result of their reduced distance in this configuration. Overall, the similar energies for the disordered structures support the local structural motives obtained from the pair distribution function analysis in which site disorder seems to be prevalent.

2.4. The Influence of Synthesis on the Ionic Transport

In order to determine the influence of the observed local disorder and local distortions on the ionic diffusion behavior, temperature-dependent impedance spectroscopy was used to assess the ionic transport properties of the differently prepared samples. **Figure 6**a shows a representative Nyquist plot of the ball-milled Li_3ErCl_6 after a subsequent annealing time of 1 h. The data can be fit with an equivalent circuit consisting of one parallel constant phase element (CPE)/resistor in series with a CPE, representing the gold-blocking electrodes. The resolvable impedance spectra exhibit α-values of >0.9, representing the ideality of the CPE,[42] and geometric capacitances around 48×10^{-12} F cm^{-2}. Bulk and grain boundary contributions cannot be deconvoluted; however, the obtained ideality of the semicircle and capacitances corresponds well with bulk transport.[43]

Due to the significant differences in the ionic conductivity, a comparison of all acquired room-temperature impedance responses for the differently prepared samples is best shown

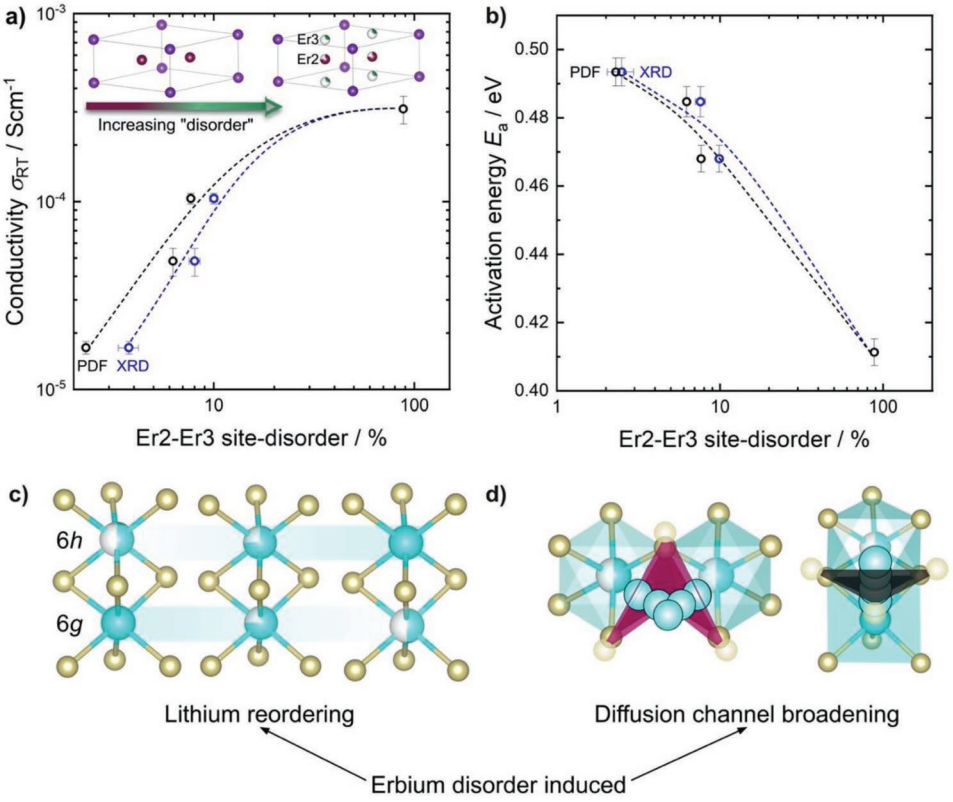

Figure 7. a,b) Evolution of the ionic conductivity and the activation barrier with increasing Er2–Er3 site disorder. c) Overall, an increased erbium occupancy in the (001) plane likely leads to a reordering of the lithium substructure, due to the increased Coulombic repulsion in this plane (Wyckoff 6g position) and potentially creates further vacant sites. d) The decreasing activation barrier can likely be related to a change of the bottlenecks for lithium diffusion.

in double logarithmic Nyquist plots, normalized to the pellet thickness for better comparison (see Figure 6b). The obtained Arrhenius diagrams can be found in Figure 6c with the calculated activation energies for ion migration and the corresponding room temperature ionic conductivities in Figure 6d. The linear behavior of the Arrhenius plots, as well as the low uncertainty for the transport property values corroborate a good fit quality. With increasing annealing time, an increase of the activation energy can be observed that coincides with a decrease of the ionic conductivity. The ionic conductivity for these chemically identical compounds can range from $1.7(1) \times 10^{-5}$ S cm^{-1} (ampoule synthesis) to $3.1(5) \times 10^{-4}$ S cm^{-1} (ball-milled, as-prepared sample), showing the importance and influence of the employed synthesis method.

2.5. Cation-Disorder-Dependent Ion Conductivity

The above-shown data clearly show a significant influence of the synthesis procedure on the ordering of erbium in the structure, along with strong distortions in the polyhedral pathways and changes in the ionic transport. The following structure–transport correlations may be inferred:

1) During the harsh mechanochemical synthesis (ball-milling) a site disorder of Er2 and Er3 can be found, which decreases with increasing annealing time. Density functional calculations show that the disordering has similar thermodynamic stabilities and the experimental data show that the annealing always leads to a high Er2 occupation (Supporting Information). It remains to be seen if changes in the annealing temperatures and times can influence the disorder further.
2) A direct correlation of the Er2–Er3 site disorder on the ionic conductivity can be seen as shown in **Figure 7**a. With increasing disorder, the conductivity increases. It is likely that this stems from an induced lithium reordering due to the Coulombic repulsion with the disordered erbium as suggested in Figure 7c. The reordering would change the effective carrier density in both planes and significantly affect the transport mechanism. Temperature-dependent neutron diffraction data and extensive ab initio molecular dynamics simulation are necessary to locate the lithium positions and changing occupancies between the different synthesis methods in order to probe the influence of cation disorder on the lithium migration pathways.
3) A direct correlation of the Er2–Er3 site disorder and the obtained activation barrier for ion migration can be observed in Figure 7b. Due to the milling and the occurring site disorder, severe local distortions can be found that can affect the structural windows of the ion jump, as discussed in Figure 4b. A correlation of the activation barriers with the changing bottleneck sizes along the diffusion pathway in the *z*-direction in Li_3ErCl_6 is shown in Figure S13 (Supporting Information). As shown for multiple different material

classes, a changing of the structural bottleneck areas leads to a decreasing activation energy and is related to the lower necessary anion displacement during lithium diffusion from one to another vacant site.[9,15,44]

3. Conclusion

In this work, we report the influence of the synthetic procedure on the structure and ionic transport properties of Li_3ErCl_6 and Li_3YCl_6. Using the highly amorphous phases after mechanochemical synthesis, Li_3ErCl_6 and Li_3YCl_6 can be crystallized, within an annealing time of 1 and 5 min, respectively. By monitoring the structural differences via Rietveld refinement against X-ray diffraction data and pair distribution functions analyses the structural differences were explored. A prevalent site disorder can be found between the Er/Y sites alongside with other local changes such as $LiCl_6^{5-}$ octahedral distortion that result in changing polyhedral-transition areas. A large degree of disordering occurs during the mechanochemical synthesis, i.e., an almost complete site inversion from the *M*2 to the *M*3 site. The subsequent annealing leads to a crystallization and partial reordering between those sites and an effective temporal dependence of the ordering. This in turn affects the ionic transport, where the disordered and distorted structure as obtained from the mechanochemical synthesis shows significantly enhanced transport properties by expanding bottlenecks for lithium diffusion and a possible reordering of the lithium sublattice corresponding to the *M*2–*M*3 disorder. This work highlights the importance of the employed synthesis approach on the ionic transport in lithium-conducting halides, as it shows that differences in the synthetic procedure can severely affect the structure and resulting diffusion pathways in superionic conductors.

4. Experimental Section

Synthesis: The preparation for all compounds was carried out under Ar atmosphere. LiCl (Alfa Aesar, 99.9%), $ErCl_3$ (Sigma Aldrich, 99%), and YCl_3 (Alfa Aesar, 99.999%) were used as received. 1 g batches were prepared while using around 10 wt% excess of the rare-earth halide to compensate for the losses during the pregrinding step in an agate mortar due to the strong adhesion between the rare-earth halide precursor and the agate mortar. The 10 wt% excess of the rare-earth halide was set by phase purity analyses of the resulting compounds. The hand ground mixtures were either pressed into dense pellets before filling them into ≈10 cm long quartz ampoules (10 mm inner diameter) for the classic solid-state synthesis or put into 45 mL ball mill cups using a 30:1 mass ratio for 3 mm ZrO_2 milling media: precursor powder for the mechanochemical synthesis. Every ampoule was preheated under dynamic vacuum at 800 °C for at least 1.5 h and every ball mill cup dried for at least 12 h at 60 °C under dynamic vacuum, to ensure the removal of all traces of water. The ampoules containing the powder mixture were sealed under vacuum before the reactions were carried out at 550 °C for one week. The mechanochemical reactions were carried out for a total of 297 cycles using three subsequent steps of 99 cycles each, with a cycle consisting of a milling time of 5 min at 500 rpm, followed by a rest step of 15 min. After each cycle, the mixture was homogenized to ensure the absence of reaction hot spots. For the crystallization, the ampoules were placed into the preheated furnace and were afterward air-quenched to ensure precise annealing times. Annealing was done in the aforementioned ampoules at 550 °C with an annealing time of 1 min (5 min in the case of Li_3YCl_6) or 1 h, respectively.

X-Ray Diffraction and Structural Analysis: X-ray diffraction was carried out at room temperature with a STOE STADI P Mythen2 4K diffractometer (Ge(111) monochromator; Ag Kα_1 radiation, $\lambda = 0.5594$ Å) using four Dectris MYTHEN2 R 1K detector in Debye–Scherrer geometry. For more information on this dedicated diffractometer for pair distribution function analyses, please see ref. [45]. All samples were sealed in glass capillaries (Ø = 0.5 mm) prior to measurement collection, which was carried out in the *Q*-range of 0.3–20.5 Å^{-1}. Measurements were carried out for 6 h for the crystalline samples and precursors and 22 h for the amorphous (as-prepared, ball-milled) sample.

Rietveld refinements were carried out using the TOPAS software package.[46] Due to the lab X-ray diffractometer the X-ray diffraction patterns exhibit an asymmetry at the low angle side of the reflections, however, structural refinements are possible when accounting for the asymmetry. The fit indicator goodness-of-fit (GOF) and a visual assessment were used to determine the quality of the fits. A Chebyshev function of ten parameters was used to fit the background and the peak shape modeling was performed using a modified Thomson–Cox–Hastings pseudo-Voigt function. The initial profile fit included: 1) background coefficients, and scale factor, followed by 2) peak shape and lattice parameters. The Rietveld analyses included: 3) erbium and chloride atomic coordinates, while ensuring an octahedral coordination for erbium with a constraint for the chlorine atomic coordinates. Finally, 4) isotropic atomic displacement parameters for erbium and chlorine and 5) disorder between the Er2 and Er3 sites were refined. Different disorder models were tested, including further Wyckoff positions for erbium (1b, 2c, 3e, 3f) and especially an antisite disorder where erbium occupies lithium positions and vice versa. All of those trials resulted in no apparent occupancy of erbium on any other site than the later shown Er1, Er2, and Er3 sites. Finally, all open parameters were refined together. Due to the low scattering form factor of lithium for X-rays, a refinement of lithium-related values was not possible. The used constraints and refinement results are provided in Table S3 (Supporting information).

The PDF was calculated by Fourier-transforming the obtained normalized structure function *S*(*Q*) using PDFgetX3. Although the pair distribution function shows no change for the crystalline samples in a *Q*-range cutoff of 12–17 Å^{-1}, the pair distribution function for the ball-milled (as prepared) sample becomes significantly worse with increasing *Q*-range cutoff. Therefore, a *Q*-range cutoff of 12 Å^{-1} was chosen for all samples, to ensure the best possible comparability.

In case of all crystalline samples, the fits were carried out using PDFGui.[47] The instrumental resolution parameter q_{damp} (0.011) and q_{broad} (0.010) corresponding to the used instrument are known from a LaB_6 standard.[45] After accounting for the background and sample absorption, the initial refinement included: 1) the scale factor and the atomic correlated motion factor,[48] followed by 2) the lattice parameters. 3) The chloride and erbium atomic coordinates were refined with symmetry constraints corresponding to the P$\bar{3}$m1 space group. It is worth mentioning that the symmetry constrained atomic coordinates (XRD refinement, Table S3, Supporting Information) split when using the data processing of PDFGui (see Figure S3, Supporting Information). For the erbium position, this results in a conversion from 3 to 5 positions and for the chloride anions from 3 to 18 positions (3 stacks of 6 positions each due to the octahedral coordination for erbium), which allows for a slight displacement of the chlorine positions out of the P$\bar{3}$m1 symmetry. 4) The atomic displacement parameters for each of the 5 erbium positions were constrained to be equal, and the atomic displacement parameters for the chloride anion were constrained to be equal for every stack of 6 positions each, corresponding to a similar behavior for every $ErCl_3^{3-}$ octahedra. An example for the position splitting and the employed constraints is shown as a schematic in Figure S3 (Supporting Information). Finally, 5) the Er2–Er3 disorder was refined, starting from the fully ordered structure (Er2 occupancy = 100%). These constraints are similar to the ones from the Rietveld refinement while additionally allowing for a slight local symmetry reduction and keeping chemically reasonable coordination for every element. As the pair distribution

function was calculated from the X-ray diffraction pattern, the lithium-related values were not refined. For the crystalline samples, a *r*-range of 20 Å was refined in the pair distribution function, corresponding to the unit cell diagonal distance.

Due to its amorphous nature and resulting lower coherence length, two different ranges of 2–8 Å (highly local) and 2–20 Å (more average) were fit for the ball-milled (as-prepared) sample, to gain insight into different features of the of Li_3ErCl_6 structure. Although a fit for a *r*-range of 20 Å was also performed and is shown in Figure S4 (Supporting Information), the structure obtained from the lower 8 Å *r*-range fit was used for the upcoming discussion, to correlate the observed behavior to the highly local structural changes. The experimental pair distribution function for both ranges was fitted by the sum of a Li_3ErCl_6 and a precursor $ErCl_3$ contribution. As a starting model, the crystal structures of Li_3ErCl_6 and $ErCl_3$ as obtained by Rietveld refinements against collected X-ray diffraction data were used. The atomic displacement parameters were refined with PDFgui and set constant in the DiffPy-CMI fit afterward.[49] The correlated motion parameter, occupancy of the Er2/Er3 positions, *z*-coordinates of the Er2/Er3 atoms, and *x,y,z*-coordinates of the Cl atoms, constrained to an octahedral geometry respective to the Er center cation, were refined in Diffpy-CMI. The two phases $ErCl_3$ and Li_3ErCl_6 were each considered in the fit with their own scaling factor (mc1, mc2), while $G(r)_i$ is the partial pair distribution function of phase p_i and $G(r)_{total}$ the sum of the two scaled partial PDFs

$$\begin{aligned} &mc1 * G(r)_{ErCl_3} + mc2 * G(r)_{Li_3ErCl_6} = G(r)_{total} \\ &mc1 = \text{molar content } Li_3ErCl_6 \\ &mc2 = \text{molar content } ErCl_3 \end{aligned} \quad (1)$$

The scaling factors for the two phases provide the molar ratio $ErCl_3$:Li_3ErCl_6. A refinement including the second precursor phase LiCl as a third phase did not result in any observable contributions to the fit, possibly due to a low scattering form factor, and was therefore excluded for the final fits. The scaling factors and calculated molar ratio of both phases can be found in Table S1 (Supporting Information).

Whereas refinements of the $G(r)$ of Li_3ErCl_6 are possible, a large fluorescence-like behavior was observed for Li_3YCl_6 that resulted in a bad signal-to-noise ratio and the appearance of termination ripples that cannot be accounted for during fitting (see Figures S1 and S5, Supporting Information). Although the pair distribution function can still be described by the same structure as used for Li_3ErCl_6, the aforementioned issues result in high fit residuals and therefore no quantitative pair distribution function analysis of Li_3YCl_6 will be included in the discussion, however, a qualitative comparison is still possible.

DFT Calculations: All calculations were performed within the framework of the density functional theory based on the Perdew–Burke–Ernzerhof (PBE) generalized gradient approximations[50] as implemented in the VASP package.[51] The core electrons were treated within the projector augmented wave (PAW) method.[52] A 3 × 3 × 3 Monkhorst–Pack k-point mesh was used on the 1 × 1 × 2 supercell of Li_3ErCl_6. The lattice parameters were kept at the experimental values while atomic positions are relaxed until the forces on all atoms were smaller than 10^{-4} eV Å^{-1}. A 520 eV plane-wave energy cutoff was used for all calculations. To remove partial occupancies on Li and Er sites, the Ewald summation as implemented in Pymatgen package[53] was used to compute the electrostatic energy of different configurations of Li and Er ions in the structure. Ten structures with different symmetries and lowest electrostatic energy were recomputed with DFT to get a more accurate ground-state energy.

Electrochemical Impedance Spectroscopy (EIS): Electrical conductivities were measured using AC impedance spectroscopy, using consolidated pellets with a thickness of ≈2 mm and a geometric density of >85% packed into argon-filled pouch cells. The pellets (0.79 cm^2) were initially hand pressed and afterward isostatically pressed at ≈360 MPa for 45 min. Evaporated gold electrodes (0.53 cm^2) were used for contacting. EIS was conducted in the temperature range of –40 to 60 °C using a VMP300 impedance analyzer (Biologic) at a frequency range of 7 MHz to 100 mHz with an excitation amplitude of 10 mV.

Supporting Information

Supporting Information is available from the Wiley Online Library or from the author.

Acknowledgements

The research was supported by the Deutsche Forschungsgemeinschaft (DFG) under Grant No. ZE 1010/4-1. N.P. and M.Z. thank Kirsten MO Jensen for support in diffpy-cmi modeling.

Conflict of Interest

The authors declare no conflict of interest.

Keywords

mechanochemical synthesis, solid electrolyte, solid-state battery, superionic conductor

Received: November 12, 2019
Revised: December 2, 2019
Published online: December 17, 2019

[1] J. Janek, W. G. Zeier. *Nat. Energy* **2016**, *1*, 16141.
[2] Y. Kato, S. Hori, T. Saito, K. Suzuki, M. Hirayama, A. Mitsui, M. Yonemura, H. Iba, R. Kanno, *Nat. Energy* **2016**, *1*, 16030.
[3] A. Manthiram, X. Yu, S. Wang, *Nat. Rev. Mater.* **2017**, *2*, 16103.
[4] E. J. Cussen, *J. Mater. Chem.* **2010**, *20*, 5167.
[5] D. Rettenwander, G. Redhammer, F. Preishuber-Pflügl, L. Cheng, L. Miara, R. Wagner, A. Welzl, E. Suard, M. M. Doeff, M. Wilkening, J. Fleig, G. Amthauer, *Chem. Mater.* **2016**, *28*, 2384.
[6] Y. Li, J. T. Han, C. A. Wang, S. C. Vogel, H. Xie, M. Xu, J. B. Goodenough, *J. Power Sources* **2012**, *209*, 278.
[7] R. Murugan, V. Thangadurai, W. Weppner, *Angew. Chem., Int. Ed.* **2007**, *46*, 7778.
[8] D. A. Weber, A. Senyshyn, K. S. Weldert, S. Wenzel, W. Zhang, R. Kaiser, S. Berendts, J. Janek, W. G. Zeier, *Chem. Mater.* **2016**, *28*, 5905.
[9] T. Krauskopf, S. P. Culver, W. G. Zeier, *Chem. Mater.* **2018**, *30*, 1791.
[10] S. P. Ong, Y. Mo, W. D. Richards, L. Miara, H. S. Lee, G. Ceder, *Energy Environ. Sci.* **2013**, *6*, 148.
[11] A. Kuhn, O. Gerbig, C. Zhu, F. Falkenberg, J. Maier, B. V. Lotsch, *Phys. Chem. Chem. Phys.* **2014**, *16*, 14669.
[12] N. Kamaya, K. Homma, Y. Yamakawa, M. Hirayama, R. Kanno, M. Yonemura, T. Kamiyama, Y. Kato, S. Hama, K. Kawamoto, A. Mitsui, *Nat. Mater.* **2011**, *10*, 682.
[13] H. J. Deiseroth, S. T. Kong, H. Eckert, J. Vannahme, C. Reiner, T. Zaiß, M. Schlosser, *Angew. Chem., Int. Ed.* **2008**, *47*, 755.
[14] P. Adeli, J. D. Bazak, K. H. Park, I. Kochetkov, A. Huq, G. R. Goward, L. F. Nazar, *Angew. Chem., Int. Ed.* **2019**, *58*, 8681.
[15] R. Schlem, M. Ghidiu, S. P. Culver, A. L. Hansen, W. G. Zeier, *Appl. Energy Mater.* **2019**, https://doi.org/10.1021/acsaem.9b01794.
[16] M. A. Kraft, S. Ohno, T. Zinkevich, R. Koerver, S. P. Culver, T. Fuchs, A. Senyshyn, S. Indris, B. J. Morgan, W. G. Zeier, *J. Am. Chem. Soc.* **2018**, *140*, 16330.
[17] A. Hayashi, S. Hama, T. Minami, M. Tatsumisago, *Electrochem. Commun.* **2003**, *5*, 111.
[18] C. Dietrich, D. A. Weber, S. J. Sedlmaier, S. Indris, S. P. Culver, D. Walter, J. Janek, W. G. Zeier, *J. Mater. Chem. A* **2017**, *5*, 18111.

[19] A. Hayashi, S. Hama, H. Morimoto, M. Tatsumisago, T. Minami, *J. Am. Ceram. Soc.* **2004**, *84*, 477.
[20] M. Tatsumisago, S. Hama, A. Hayashi, H. Morimoto, T. Minami, *Solid State Ionics* **2002**, *154*, 635.
[21] A. Hayashi, S. Kama, F. Mizuno, K. Tadanaga, T. Minami, M. Tatsumisago, *Solid State Ionics* **2004**, *175*, 683.
[22] T. Minami, A. Hayashi, M. Tatsumisago, *Solid State Ionics* **2006**, *177*, 2715.
[23] S. P. Culver, R. Koerver, T. Krauskopf, W. G. Zeier, *Chem. Mater.* **2018**, *30*, 4179.
[24] M. Ghidiu, J. Ruhl, S. P. Culver, W. G. Zeier, *J. Mater. Chem. A* **2019**, *7*, 17735.
[25] Y. Kato, S. Shiotani, K. Morita, K. Suzuki, M. Hirayama, R. Kanno, *J. Phys. Chem. Lett.* **2018**, *9*, 607.
[26] Y. Zhu, X. He, Y. Mo, *ACS Appl. Mater. Interfaces* **2015**, *7*, 23685.
[27] W. D. Richards, L. J. Miara, Y. Wang, J. C. Kim, G. Ceder, *Chem. Mater.* **2016**, *28*, 266.
[28] G. F. Dewald, S. Ohno, M. A. Kraft, R. Koerver, P. Till, N. M. Vargas-Barbosa, J. Janek, W. G. Zeier, *Chem. Mater.* **2019**, *31*, 8328.
[29] R. Koerver, I. Aygün, T. Leichtweiß, C. Dietrich, W. Zhang, J. O. Binder, P. Hartmann, W. G. Zeier, J. Janek, *Chem. Mater.* **2017**, *29*, 5574.
[30] A. Sakuda, A. Hayashi, M. Tatsumisago, *Sci. Rep.* **2013**, *3*, 2261.
[31] T. Asano, A. Sakai, S. Ouchi, M. Sakaida, A. Miyazaki, S. Hasegawa, *Adv. Mater.* **2018**, *30*, 1803075.
[32] S. Wang, Q. Bai, A. M. Nolan, Y. Liu, S. Gong, Q. Sun, Y. Mo, *Angew. Chem., Int. Ed.* **2019**, *58*, 8039.
[33] S. Muy, J. Voss, R. Schlem, R. Koerver, S. J. Sedlmaier, F. Maglia, P. Lamp, W. G. Zeier, Y. Shao-Horn, *iScience* **2019**, *16*, 270.
[34] Z. Xu, X. Chen, K. Liu, R. Chen, X. Zeng, H. Zhu, *Chem. Mater.* **2019**, *31*, 7425.
[35] X. Li, J. Liang, J. Luo, M. N. Banis, C. Wang, W. Li, S. Deng, C. Yu, F. Zhao, Y. Hu, T. Sham, L. Zhang, S. Zhao, S. Lu, H. Huang, R. Li, K. R. Adair, X. Sun, *Energy Environ. Sci.* **2019**, *12*, 2665.
[36] A. W. Atkinson, J. R. Chadwick, E. Kinsella, *J. Inorg. Nucl. Chem.* **1968**, *30*, 401.
[37] H.-J. Steiner, H. D. Lutz, *Z. Anorg. Allg. Chem.* **1992**, *613*, 26.
[38] A. Bohnsack, F. Stenzel, A. Zajonc, G. Balzer, M. S. Wickleder, G. Meyer, *Z. Anorg. Allg.* **1997**, *623*, 1067.
[39] R. D. Shannon, *Acta Crystallogr.* **1976**, *A32*, 751.
[40] A. Gautam, M. Sadowski, N. Prinz, H. Eickhoff, N. Minafra, M. Ghidiu, S. P. Culver, K. Albe, T. F. Fässler, M. Zobel, W. G. Zeier, *Chem. Mater.* **2019**, https://doi.org/10.1021/acs.chemmater.9b03852.
[41] Y. Wang, W. D. Richards, S. P. Ong, L. J. Miara, J. C. Kim, Y. Mo, G. Ceder, *Nat. Mater.* **2015**, *14*, 1026.
[42] G. J. Brug, A. L. G. van den Eeden, M. Sluyters-Rehbach, J. H. Sluyters, *J. Electroanal. Chem.* **1984**, *176*, 275.
[43] A. West, J. Irvine, D. Sinclair, *Adv. Mater.* **1990**, *2*, 132.
[44] J. C. Bachman, S. Muy, A. Grimaud, H. H. Chang, N. Pour, S. F. Lux, O. Paschos, F. Maglia, S. Lupart, P. Lamp, L. Giordano, Y. Shao-Horn, *Chem. Rev.* **2016**, *116*, 140.
[45] S. L. J. Thomae, N. Prinz, T. Hartmann, M. Teck, S. Correll, M. Zobel, *Rev. Sci. Instrum.* **2019**, *90*, 043905.
[46] A. A. Coelho, *J. Appl. Crystallogr.* **2018**, *51*, 210.
[47] P. Juhás, T. Davis, C. L. Farrow, S. J. L. Billinge, *J. Appl. Crystallogr.* **2013**, *46*, 560.
[48] I. K. Jeong, R. H. Heffner, M. J. Graf, S. J. L. Billinge, *Phys. Rev. B: Condens. Matter Mater. Phys.* **2003**, *67*, 9.
[49] P. Juhás, C. L. Farrow, X. Yang, K. R. Knox, S. J. L. Billinge, *Acta Crystallogr., Sect. A: Found. Adv.* **2015**, *71*, 562.
[50] J.P. Perdew, K. Burke, M. Ernzerhof, *Phys. Rev. Lett.* **1996**, *77*, 3865.
[51] G. Kresse, J. Furthmüller, *Phys. Rev. B: Condens. Matter Mater. Phys.* **1996**, *54*, 11169.
[52] P. E. Blöchl, *Phys. Rev. B* **1994**, *50*, 17953.
[53] S. P. Ong, W. D. Richards, A. Jain, G. Hautier, M. Kocher, S. Cholia, D. Gunter, V. L. Chevrier, K. A. Persson, G. Ceder, *Comput. Mater. Sci.* **2013**, *68*, 314.